Systems & Control Transactions

Original Research Article
Peer Reviewed Conference Proceeding
ESCAPE 36 - European Symposium on Computer Aided Process Engineering
Sheffield, UK. 21-24 June 2026

PSE PRESS

An Open-Source IDAES Framework for Simulating Inductively Heated Adsorption Processes

Sudip Sharma[a], Thomas A. Adams II[a]*

[a] Norwegian University of Science and Technology (NTNU), Department of Energy and Process Engineering, Trondheim, Norway
* Corresponding Author: thomas.a.adams@ntnu.no

ABSTRACT

Magnetic Inductive Swing Adsorption (MISA) is a carbon dioxide capture process similar to Temperature Swing Adsorption that uses direct electromagnetic heating instead of classic heating systems for the regeneration step of the process. However, the lack of validated dynamic models hinders process optimization. This work introduces an open-source MISA model in the IDAES framework, incorporating Specific Absorption Rate (SAR) physics (SAR $\propto B^2$) to capture electromagnetic heating. Binary Sips isotherm parameters for Fe_3O_4@HKUST-1 were fitted to experimental data, achieving high statistical agreement (R2 > 0.996, RMSE < 0.022 mol/kg). Comprehensive validation was performed against adsorption isotherms, dynamic breakthrough curves, and desorption profiles. The model predicts breakthrough time with only 9% error and saturation time with 6% error. Crucially, the coupled thermal transport and SAR heating model capture temperature evolution during desorption within 5% error across all field strengths. Although the use of Linear Driving Force kinetics introduces minor systematic overprediction, the model successfully bridges the gap between laboratory feasibility and industrial design. This validated tool enables the first systematic investigation of cycle configurations, providing a platform for techno-economic comparisons and scale-up of energy-efficient magnetic carbon capture.

Keywords: Carbon Capture, Adsorption, Modelling and Simulations, Metal Organic Framework (MOF)

1. INTRODUCTION

Mitigating anthropogenic carbon dioxide emissions remains critical for achieving global climate targets, with post-combustion carbon dioxide (CO_2) capture representing a key near-term strategy for industrial decarbonization [1]. Traditional Temperature Swing Adsorption (TSA) processes regenerate solid adsorbents through external heating, but suffer from fundamental limitations; poor thermal conductivity creates temperature gradients, slow heat penetration extends cycle times, and thermal resistances cause energy losses often exceeding 3-4 GJ/tonne CO_2 [2].

Magnetic Inductive Swing Adsorption (MISA) addresses these limitations through direct volumetric heating of magnetic nanoparticles embedded in adsorbent materials [2]. When exposed to alternating magnetic fields, Fe_3O_4 nanoparticles generate heat through hysteresis and relaxation mechanisms, bypassing thermal resistances inherent in conventional TSA. Bellusci *et al.* [2] demonstrated that Fe_3O_4@HKUST-1 composites achieve 95% CO_2 recovery in about 2.5 minutes, almost four times faster than Temperature Swing Adsorption (TSA) [2].

Despite experimental demonstrations of MISA feasibility, validated dynamic models for process design remain lacking. Existing fixed-bed models in process simulation frameworks do not include electromagnetic heating capabilities, and proprietary models are not publicly available. This absence of validated open-source tools represents a barrier to systematic exploration of MISA cycle configurations and scale-up necessary for industrial implementation.

This work presents a new, validated open-source MISA model using the Institute for the Design of Advanced Energy Systems (IDAES) framework [3]. The model extends the standard `FixedBed1D` class with Specific Absorption Rate (SAR) physics for electromagnetic heating. Binary Sips isotherm parameters were fitted to experimental data [2, 4] using Python Adsorption Parameter Estimation Package (pyAPEP) [5], achieving R^2 >

0.996 for both CO_2 and Nitrogen (N_2). Comprehensive validation was performed against three independent datasets: adsorption isotherms (273-403 K), dynamic breakthrough curves (15-50% CO_2), and magnetic desorption profiles (11.1-12.6 mT). The validated implementation enables systematic investigation of cycle design and optimization, providing the computational foundation for techno-economic analysis and scale-up studies.

2. MATERIALS AND METHODS

2.1 Adsorbent Material and Isotherms

The adsorbent material used in this study is a Fe_3O_4@HKUST-1 magnetic composite developed by Bellusci *et al.* [2]. This material consists of the metal organic framework (MOF) HKUST-1 ($Cu_3(BTC)_2$) impregnated with 17 wt% magnetite (Fe_3O_4) nanoparticles. The magnetic nanoparticles enable direct heating of the solid phase through electromagnetic induction, while MOF provides high CO_2 adsorption capacity.

The adsorption equilibrium for both CO_2 and N_2 was modeled using the Sips isotherm, which combines Langmuir and Freundlich characteristics:

$$q_{(eq,i)(T,P_i)} = \frac{n_{\infty,i}(b_i(T)\,P_i)^{c_i}}{1+(b_i(T)\,P_i)^{c_i}} \quad (1)$$

where $q_{(eq,i)}$is the adsorbed amount of component i (mol/kg), $n_{\infty,i}$ is saturation capacity, $b_i(T)$ is the affinity parameter as a function of T, c_i is the heterogeneity parameter, and P_i is the partial pressure. The affinity parameter exhibits temperature dependence according to:

$$b_i(T) = b_{ref,i}\exp\left[\frac{\Delta H_{b,i}}{R}\left(\frac{1}{T_{ref}}-\frac{1}{T}\right)\right] \quad (2)$$

where $\Delta H_{b,i}$ is the isosteric heat of adsorption and T_{ref} = 298 K.

Experimental adsorption isotherms for both CO_2 and N_2 were obtained from Bellusci *et al.* [2, 4] by manual extraction of gas uptake (mol/kg) versus pressure (kPa) data across multiple temperatures (273-403 K for CO_2, 273-308 K for N_2) using a plot digitation tool. The extracted dataset served as the training set for parameter estimation.

The binary Sips isotherm parameters were determined through nonlinear regression using pyAPEP [5], which performs global nonlinear regression to simultaneously optimize all parameters.

Figure 1 demonstrates excellent agreement between the fitted model and experimental data. The fitted parameters (Table 1) reveal the expected selectivity: CO_2 exhibits significantly higher saturation capacity. The heats of adsorption (ΔH_b = 23.5 kJ/mol for CO_2, 15.3 kJ/mol for N_2) are physically reasonable for physisorption and correctly predict decreased loading with increasing temperature and is close to the experimental value of 23 kJ/mol for CO_2 [2]. The validated isotherm provides the thermodynamic foundation for all subsequent dynamic simulations.

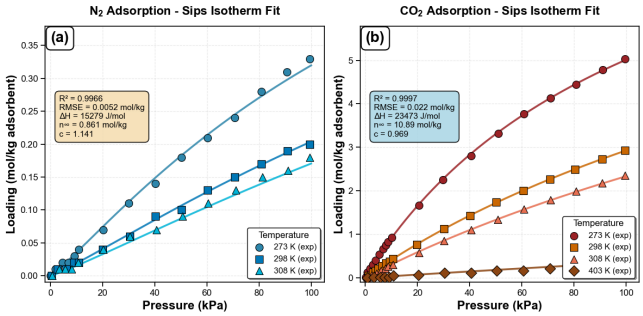

Figure 1. Validation of Sips isotherm model against experimental adsorption data from Bellusci et al. [2, 4]. (a) N_2 adsorption (273-308 K, R^2=0.9970). (b) CO_2 adsorption (273-403 K, R^2=0.9997). Lines: model predictions; symbols: experimental measurements.

Table 1 presents the fitted parameters along with statistical measures of goodness-of-fit. The high R^2 values (>0.996) and low RMSE values indicate excellent agreement with data across the measured temperature and pressure ranges (298 – 403K, 0.01-100 kPa). Details are available in the supplementary material.

Table 1. Sips Isotherm Parameters found

Parameter	CO_2	N_2	Unit
n_∞	10.89	0.926	mol/kg
b_{ref}(298K)	4.24 × 10^{-6}	1.57 × 10^{-6}	Pa^{-1}
c	0.969	1.128	–
ΔH_b	23, 473	15, 184	J/mol
R^2	0.9997	0.997	–
$RMSE$	0.022	0.0049	mol/kg

2.2 Mathematical Model

2.2.1 System Description and Assumptions

The Magnetic Inductive Swing Induction process is modeled as a one-dimensional fixed bed adsorber operated in transient mode. The model captures the coupled dynamics of gas flow, heat transfer, and adsorption/desorption in a cylindrical packed bed containing Fe_3O_4@HKUST-1 composite adsorbent. The key modeling assumptions are:

- **One-dimensional plug flow:** Radial concentration and temperature gradients are negligible compared to axial variations
- **Dynamic operation:** Transient behavior captured through time-dependent terms
- **Two-phase system** with local thermal non-equilibrium between gas and solid phases

- **Ideal gas behavior:** Gas mixture obeys the ideal gas law
- **Uniform bed properties:** Bed porosity and particle size throughout the bed
- **Linear driving force (LDF) kinetics:** Adsorption rate proportional to difference between equilibrium and actual loading
- **Negligible axial dispersion:** Convective transport dominates over diffusive/dispersive transport in the gas phase
- **Local pressure equilibrium:** Pressure within particle pores instantly equilibrates with the bulk gas pressure

2.2.2 Conservation Equations -Standard Framework

We implemented the model in IDAES using the `FixedBed1D` class, which generates standard conservation equations [6]. The governing equations include:

Gas phase material balance for each component i (CO_2, N_2):

$$A_b \cdot \varepsilon_b \cdot \frac{\partial(\rho_{mol} \cdot y_i)}{\partial t} = -\frac{\partial(F_{mol,i})}{\partial x} - A_s \cdot \rho_p \cdot r_{ads,i} \quad (3)$$

Gas phase energy balance:

$$A_b \cdot \varepsilon_b \cdot \frac{\partial(\rho_{mol} \cdot h_{mol,g})}{\partial t} = -\frac{\partial H_g}{\partial x} - \frac{6h_{gs}}{d_p} \cdot A_s \cdot (T_g - T_s) \quad (4)$$

Momentum Balance (Ergun Equation):

$$-\frac{dP_g}{dx} = \frac{150\mu_i(1-\varepsilon_b)^2 u}{\varepsilon_b{}^3 d_p^2} + \frac{1.75\rho_g(1-\varepsilon_b)u^2}{\varepsilon_b{}^3 d_p} \quad (5)$$

Solid Phase material balance for adsorbed component i:

$$A_s \cdot \rho_p \cdot \frac{\partial(q_i)}{\partial t} = A_s \cdot \rho_p \cdot r_{ads,i} \quad (6)$$

where geometric parameters include bed porosity ε_b[-], bed cross-sectional area A_b $[m^2]$, solid cross-sectional area $A_s = (1-\varepsilon_b)\,A_b$ $[m^2]$, and particle diameter $d_p[m]$. Gas phase variables include molar density ρ_{mol} $[mol/m^3]$, mass density ρ_g $[kg/m^3]$, species mole fraction y_i [-], superficial velocity u $[m/s]$, temperature T_g [K], absolute pressure P_g $[Pa]$, viscosity μ_g $[Pa \cdot s]$, and specific enthalpy $h_{mol,g}$ $[J/mol]$. Enthalpy flow rate $H_g = u \cdot A_b \cdot \rho_{mol} \cdot h_{mol,g}$ $[W]$ and species molar flow rate $F_{mol,i} = u \cdot A_b \cdot \rho_{mol} \cdot y_i$ $[mol/s]$. Solid phase variables include particle density ρ_p $[kg/m^3]$ adsorbed loading q_i $[mol/kg]$, temperature T_s $[K]$, and adsorption rate r_{ads}, i $[mol/(kg \cdot s)]$. The gas-solid heat transfer coefficient is h_{gs} $[W/(m^2 \cdot K)]$.

Bed porosity (void fraction) is calculated using the following relation [7]:

$$\varepsilon_b = 0.38 + 0.073\left[1 - \frac{\left(\frac{d_b}{d_p} - 2\right)^2}{\left(\frac{d_b}{d_p}\right)^2}\right] \quad (7)$$

where d_b is bed diameter and d_p is the particle diameter.

2.2.3 Inductive Heating Model

The key innovation extends the standard IDAES `FixedBed1D` model with inductive heating capability. When an alternating magnetic field is applied, the Fe_3O_4 nanoparticles within the composite generate heat through magnetic losses (hysteresis and relaxation mechanisms). This enables direct volumetric heating of the solid phase, bypassing the thermal resistances inherent in conventional TSA.

Specific Absorption Rate (SAR)

The heating power is characterised by the Specific Power Loss (SPL) or Specific Absorption Rate (SAR), which represents the power dissipated per unit mass of material. Based on magnetic relaxation theory[8, 9], SAR exhibits a quadratic dependence on the applied magnetic field amplitude:

$$L(B) = L_{ref}\left(\frac{B}{B_{ref}}\right)^2 \quad (8)$$

B is the applied magnetic field amplitude (mT), B_{ref} = 12.6 mT is the reference field amplitude, L is the SAR as a function of B, and L_{ref} = 1.6 W/g is the experimentally measured SAR of the Fe_3O_4@HKUST-1 composite at the reference field amplitude [2]. This quadratic scaling captures the fundamental physics of magnetic power dissipation in the superparamagnetic regime.

Modified Solid Energy balance

$$A_s \cdot \rho_p \cdot c_{p,s} \cdot \frac{\partial T_s}{\partial t} = \frac{6h_{gs}}{d_p} \cdot A_s \cdot (T_g - T_s) - A_s \cdot \rho_p \sum_i [\Delta H_{ads,i} \cdot r_{ads,i}] + Q_{ind} \cdot A_s - Q_{wall} \quad (9)$$

where Q_{ind} $[W/m^3]$ is the volumetric inductive heating rate defined in Eq. (10), $\Delta H_{ads,i}$ $[J/mol]$ is the heat of adsorption for species i (negative for exothermic adsorption), and Q_{wall} $[W/m]$ is the heat loss to ambient defined in Eq. (11)

$$Q_{ind} = L(B) \cdot \rho_p \quad (10)$$

$$Q_{wall} = h_{wall} \cdot \pi \cdot d_b \cdot (T_s - T_{ambient}) \quad (11)$$

where h_{wall} is the wall heat transfer coefficient and $T_{ambient}$ = 298 K is ambient temperature.

This formulation has three key advantages for MISA modeling:

- **Direct solid heating:** Energy is deposited directly in the solid phase, eliminating gas-to-solid heat transfer resistance
- **Controllable heating:** SAR is proportional to B^2,

allowing precise control via magnetic field amplitude

- **Rapid thermal response:** Inductive heating timescale (seconds) is much faster than conductive heating (minutes) in conventional TSA

When B = 0 (adsorption phase), Q_{ind} = 0 and the model reduces to the standard fixed-bed model but with wall heat loss. This enables modeling of complete MISA cycles where the magnetic field is switched on only during the desorption step.

2.2.4 Constitutive Relations

The model is completed with the following constitutive relations:

Adsorption equilibrium: Binary Sips isotherm (Section 2.1)

Adsorption kinetics: Linear Driving Force (LDF) model:

$$r_{ads,i} = k_i(q_{eq,i} - q_i) \qquad (12)$$

where k_i is the mass transfer coefficient, $q_{eq,i}$ is the equilibrium loading from the Sips isotherm, and $q_i$is the average solid-phase loading concentration of component i within the adsorbent particle at a given time. The mass transfer coefficient (k_{CO_2} = $0.15\ s^{-1}$) was determined by fitting experimental breakthrough curve data. The N_2 coefficient (k_{N_2} = $0.20\ s^{-1}$) was set higher than CO_2, consistent with N_2's weaker adsorption (lower heat of adsorption) and minimal contribution to overall bed dynamics due to its low saturation capacity (0.93 mol/kg vs. 10.89 mol/kg for CO_2).

Gas phase thermodynamics: Ideal gas equation of state. Pure component properties are calculated from temperature-dependent correlations: heat capacity from NIST Shomate equations [10], and while viscosity and thermal conductivity use temperature-dependent power law correlations [11]. Mixture heat capacity is calculated as mole-fraction weighted average of component values. Mixture viscosity and thermal conductivity are calculated using Wilke mixing rules [12].

Heat transfer: The gas-solid heat transfer coefficient (h_{gs}) is calculated from particle-scale Nusselt number correlations as described in the IDAES documentation [6].

2.3 Numerical Implementation

The mathematical model was implemented using IDAES framework built on the Pyomo optimization modeling environment [13]. IDAES provides standardized property package interfaces, robust initialization strategies for DAE systems, and integration with state-of-the-art solvers. The IDAES `ControlVolume1D` and `FixedBed1D` classes automatically generate standard conservation equations (material, energy, momentum), while custom constraints were implemented for inductive heating and wall heat loss.

Table 2. Model Parameters

Parameter	Value	Units
Column Geometry		
Length (L)	1.5	cm
Diameter (D)	1.0	cm
Bed porosity (ε_b)	0.39	–
Adsorbent Properties		
Particle diameter (d_p)	0.5	mm
Particle density (ρ_p)	1170	kg/m^3
Solid heat capacity ($C_{p,s}$)	1070	$J/(kg \cdot K)$
Operating Conditions - Adsorption		
Feed temperature (T_{in})	303	K
Feed pressure (P_{in})	1.3	bar
CO_2 concentration	15	$mol\%$
Molar flow rate	3.33×10^{-5}	mol/s
Magnetic field (B)	0	mT
Operating Conditions - Desorption		
Feed temperature (T_{in})	303	K
CO_2 concentration	15	$mol\%$
Molar flow rate	3.33×10^{-5}	mol/s
Magnetic field (B)	11.1 - 12.6	mT
Inductive Heating Parameters		
SAR at 12.6 mT (L_{ref})	1.6	W/g
Frequency (f)	190	kHz
Fe_3O_4 content	17	$wt\%$
Heat Transfer		
Wall heat transfer Coeff. (h_{wall})[a]	20	$W/(m^2 \cdot K)$
Ambient temperature (T_{amb})	298	K

[a] Values chosen to be in line with the literature [2, 16]

The reactor length domain (0 ≤ x ≤ L) was discretized using the backward finite difference method:

$$\frac{\partial \psi}{\partial x|_i} \approx \frac{\psi_i - \psi_{i-1}}{\Delta x} \qquad (13)$$

This discretization converts the PDEs into a DAE system in time. The backward difference scheme ensures numerical stability for convection-dominated flows and preserves causality in the flow direction.

A two-phase solution strategy was employed.

Phase 1 (Initialization): The model was initialized using hierarchical block triangularization with IPOPT [14]. State variables were temporarily fixed and constraints progressively activated in this order: thermophysical

properties, hydrodynamics, mass balances, energy balances.

Phase 2 (Dynamic Integration): The spatially discretized DAE system was integrated forward in time using the PETSc library [15] with backward Euler method:

$$\frac{\partial \psi}{\partial t}|_{n+1} \approx \frac{\psi_{n+1} - \psi_n}{\Delta t} \quad (14)$$

where Δt is the time step (adaptive). Backward Euler provides stability for stiff systems, essential for capturing fast thermal transients during inductive heating.

Table 2 summarizes the operating conditions, bed geometry, and material properties used in all simulations.

2.4 Cycle Configuration

A simple MISA process operates as a three-step cyclic process: adsorption, inductive desorption, cooling.

Step 1 – Adsorption: The regenerated bed, initially equilibrated with pure N_2 at 303 K, is exposed to the adsorption operation condition given in Table 2. CO_2 selectively adsorbs onto the Fe_3O_4@HKUST-1 composite until the bed approaches saturation, typically occurring at 135-145 seconds under the conditions in Table 2.

Step 2 - Magnetic Desorption: Upon completion of adsorption, the magnetic field is activated (B = 11.1-12.6 mT, f = 190 kHz) while maintaining the same feed flow. Electromagnetic energy is directly absorbed by the Fe_3O_4 nanoparticles, causing rapid localized heating of the solid adsorbent. This direct solid-phase heating mechanism bypasses the thermal resistances inherent in conventional TSA, where heat must be conducted through the reactor walls and gas phase. The bed temperature rises rapidly from 303 K to approximately 440 K (167°C), driving CO_2 desorption. At B = 12.6 mT (L = 1.6 W/g), approximately 95% of adsorbed CO_2 is recovered within 2.11 minutes—a 4-fold reduction compared to conventional TSA [2].

Step 3 - Cooling: The magnetic field is deactivated, and the bed is cooled by continuing gas flow (pure N_2) until thermal equilibrium is restored at 303 K. Cold N_2 (convection) and wall heat loss (h_{wall}) to ambient contribute to cooling. Once cooled, the system begins the next adsorption cycle.

This cycle configuration serves as the basis for the validation studies in Section 3.

3 MODEL VALIDATION AND DISCUSSION

The model demonstrated two independent tests: dynamic breakthrough behavior, magnetic desorption performance. This demonstration approach ensures the model accurately and captures both thermodynamic equilibrium and transport-limited dynamic behavior under both adsorption and desorption conditions.

3.1 Breakthrough Validation

Dynamic breakthrough simulations were performed to validate the coupled mass transfer and equilibrium behavior of the model under transient conditions. The breakthrough experiments reported were replicated numerically using the operating conditions in Table 2. A step change in feed composition from pure N_2 to a binary mixture (15% CO_2, 85% N_2) was introduced at t = 0 to a freshly regenerated bed initially at 303 K. The outlet CO_2 concentration was monitored until bed saturation.

3.2.1 Detailed Validation at 15% CO_2

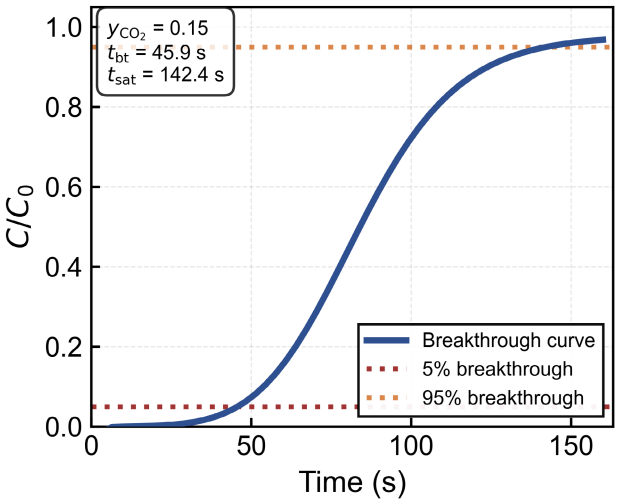

Figure 2. Solid line: model prediction. Orange dashed lines indicate the model's calculated 5% breakthrough (t = 45.9 s) and 95% saturation (t = 142.4 s) times. These are compared against the experimental benchmark values of 42 s and 138 s, respectively, as reported in the text of [2].

Figure 2 shows the high-resolution breakthrough curve validation for the 15% CO_2 feed case over a 0–160 second timeframe. Breakthrough curves express outlet concentration normalized by inlet (C/C_0). Time domain was discretized into 50 points.

Comparison with experimental data demonstrates strong agreement. The model achieves 9% error in breakthrough time and 6% error in saturation time relative to experimental values from [2]. This close agreement validates both the Sips equilibrium isotherm parameters (Table 1) and the LDF mass transfer coefficients, confirming that the model accurately captures the coupled thermodynamic and adsorptive behavior of the system.

The slight overprediction of breakthrough times may be attributed to factors like: i) the LDF approximation assumes a uniform concentration driving force within particles, while actual intraparticle profiles may be more complex [17] ii) bed channeling or radial flow maldistribution in the experimental setup, which are not captured by the 1D model [18].

3.2.2 Effect of Feed CO_2 Concentration

To further demonstrate the model's predictive capability across a wider operating range, breakthrough simulations were performed at three different CO_2 feed concentrations: 15%, 30%, and 50% (balance N_2). Figure 3 shows the simulated breakthrough curves over a 0–15 minute timeframe for all three cases. As expected, increasing CO_2 concentration results in earlier breakthrough and faster approach to saturation due to the higher driving force for adsorption and the more rapid consumption of available adsorption sites.

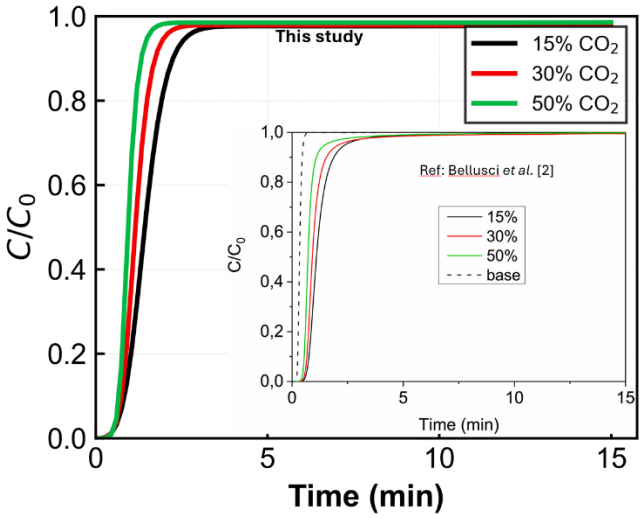

Figure 3. Breakthrough behavior at varying CO_2 feed concentrations (15%, 30%, 50%).

High-resolution experimental data for quantitative validation at 30% and 50% CO_2 were not available in [2]. However, the model captures the expected theoretical behavior: increasing the CO_2 feed concentration from 15% to 50% reduces the saturation time by a factor of 1.6. This response is consistent with the competitive adsorption physics described by the binary Sips isotherm, where higher partial pressures drive faster saturation.

3.2 Desorption Validation

Desorption simulations were performed to demonstrate the inductive heating capability and thermal coupling in the model. The desorption experiments were also replicated numerically by first saturating the bed with 15% CO_2 at 303 K, then activating the magnetic field while maintaining the same feed flow rate and composition. Three different magnetic field intensities were tested: B = 11.1, 11.8, and 12.6 mT at f = 190 kHz.

3.2.1 CO_2 Desorption Profiles

Figure 4 presents the simulated outlet CO_2 concentration profiles. Following bed saturation, the magnetic field is activated at t=0, and the outlet concentration is monitored. The peak outlet concentration reaches 28.3 vol% at 12.6 mT, demonstrating near-complete regeneration.

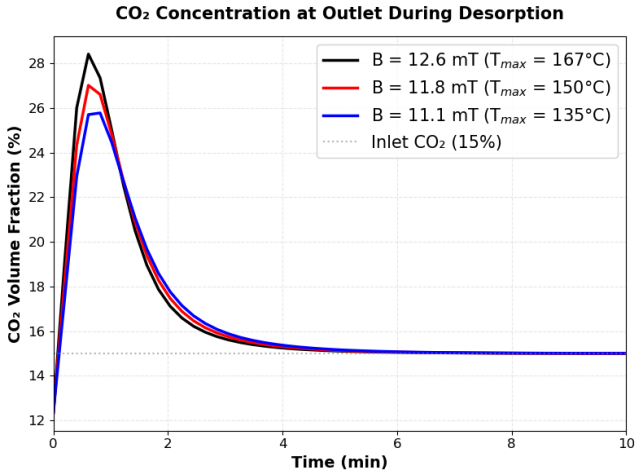

Figure 4. CO_2 desorption curve at different applied magnetic fields with maximum temperature attained at each magnetic field.

These results demonstrate the quadratic B^2 scaling relationship in the SAR model (Equation 8), consistent with Rosensweig's theory [8]. To substantiate the model's accuracy, Table 3 compares the results with experimental data from Bellusci et al. [2]. The model achieves high quantitative accuracy, predicting peak desorption magnitudes with <6% error across all field strengths. While the simulation predicts a slightly broader desorption profile due to continuum mass-transfer assumptions, the peak magnitude and total regeneration times show strong agreement with experimental values. We note that the experimental values shown in Table 3 are not precise because they were digitally determined from a low-resolution figure, so peak error is only valid to one significant figure.

Table 3. Quantitative comparison of simulated desorption against experimental data [2].

Field	Peak CO_2 (vol%)	Peak Error	Time to Peak (min)
mT	Exp./Sim.	(%)	Exp./Sim.
12.6	29.0/28.3	2	0.50/0.65
11.8	26.5/27.0	2	0.48/0.65
11.1	24.5/25.8	5	0.49/0.65

3.2.2 Temperature Evolution

Figure 5 shows the simulated bed temperature profiles during magnetic desorption for the same three field strengths. The temperature evolution directly reflects the electromagnetic heating rate determined by the SAR value. At B = 12.6 mT, the bed temperature rises rapidly from 303 K to a peak of approximately 440 K (167°C). At the lower field strengths, the peak temperatures are

proportionally lower: ~423 K (150°C) at B = 11.8 mT and ~408 K (135°C) at B = 11.1 mT.

Table 4 provides a quantitative comparison of the predicted peak temperatures against experimental measurements. The model produces close match to experimental data, with errors under 5% for all three field strengths. At the highest field strength (B = 12.6 mT), the model predicts 440 K (167°C) versus the experimental value of 448 K (175°C), representing a 4.5% error. This close agreement validates both the SAR heating model (Equation 8) and the thermal energy balance (Equation 9), confirming that the model accurately captures the coupled heat generation, accumulation, and loss mechanisms.

Table 4. Temperature and Regeneration Validation

B (mT)	T_{max} Exp.	T_{max} Model	Error (%)
12.6	448 K (175°C)	440 K (167°C)	4.5
11.8	428 K (155°C)	423 K (150°C)	3.2
11.1	403 K (130°C)	408 K (135°C)	3.8

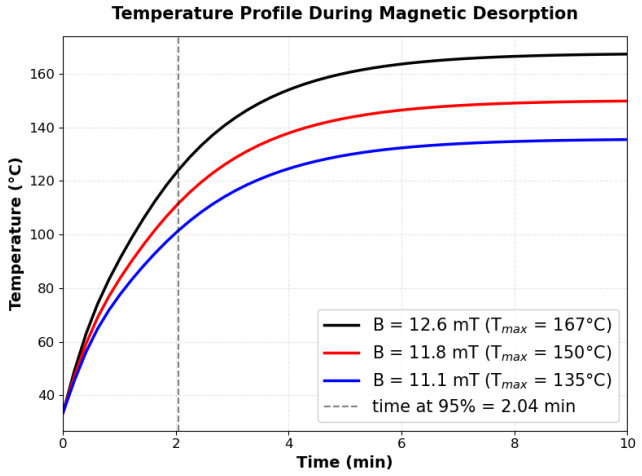

Figure 5. Temperature evolution at different B values and 95% regeneration time.

The slight underprediction of peak temperatures may be attributed to: (*i*) radial temperature gradients not captured by the 1D axial model - the thermocouple may measure local radial hot spots near the wall or center that differ from the radially-averaged temperature predicted by the 1D formulation [18], (*ii*) uncertainty in the solid heat capacity ($Cp,s = 1070\,J/(kg \cdot K)$), which was assumed constant but varies with temperature, and (*iii*) heat losses through the reactor wall (h_{wall} = 20 $W/(m^2 \cdot K)$), which may be overestimated, leading to lower predicted peak temperatures.

Despite these minor discrepancies, the strong correlation between predicted and experimental temperatures across three different field strengths confirms that the model correctly captures the physics of electromagnetic heating and thermal transport in the MISA system. The validated thermal model enables confident prediction of energy requirements and regeneration performance under various operating conditions.

3.3 Model Limitations and Applicability

While the model accurately captures thermodynamic limits, two approximations introduce kinetic deviations. First, the LDF approximation (k_i= 0.15 s^{-1}) simplifies intra-particle transport, resulting in a broader desorption profile and slower post-peak decay compared to the sharp experimental release [18]. Second, the continuum heating assumption causes a minor onset lag (~0.15 min), as volume-averaged temperatures respond slower than instantaneous local "hot spots." Despite these broadening effects, the model's thermodynamic accuracy (<6% peak error) and robust regeneration time predictions validate its utility for cycle optimization and scale-up.

4 CONCLUSION AND FUTURE WORK

This work presents the first validated open-source IDAES model for Magnetic Inductive Swing Adsorption, extending the standard `FixedBed1D` framework with electromagnetic heating capability via Specific Absorption Rate physics. Multi-level validation against experimental data confirms the model accurately captures coupled thermodynamic-kinetic-thermal behavior across different conditions for CO_2 capture (273-440 K, 15-50% CO_2, 11.1-12.6 mT), with breakthrough predictions within 9%, temperature predictions within 5%, and isotherm fits exceeding R^2 = 0.996. The validated quadratic $L \propto B^2$ scaling confirms MISA achieves four-fold faster regeneration than conventional TSA.

While the LDF kinetic approximation introduces ~10% systematic error in breakthrough times and validation remains limited to laboratory scale, the model provides a robust foundation for cycle optimization and techno-economic analysis. Future work will leverage this platform to identify optimal cycle configurations through multi-objective optimization, compare MISA economics against conventional TSA/PSA technologies, and guide scale-up to pilot demonstration.

The open-source implementation enables model extensions and facilitates MISA advancement from laboratory demonstrations toward industrial deployment for energy-efficient CO_2 capture.

ACKNOWLEDGEMENTS

This project was funded by the NTNU-MIT Energy Research Programme (project NMERP-C2).

SUPPLEMENTARY MATERIAL

Supplementary material can be downloaded at: https://PSEcommunity.org/LAPSE:2025.0725.

AUTHOR IDENTIFIERS

Author ORCIDs:
Sharma Sudip: 0000-0003-4049-6031
Adams Thomas A., II: 0000-0002-9871-9851

REFERENCES

1. Raganati F, Ammendola P. Co₂ post-combustion capture: a critical review of current technologies and future directions. Energy Fuels 38:13858-13905 (2024). https://doi.org/10.1021/acs.energyfuels.4c02513
2. Bellusci M, Albino M, Masi A, Peddis D, Innocenti C, Varsano F. High porosity-magnetic composite materials for magnetic induction swing adsorption (MISA): improvement of performance properties. Materials Chemistry and Physics 311:128525 (2024). https://doi.org/10.1016/j.matchemphys.2023.128525
3. Lee A, Ghouse JH, Eslick JC, Laird CD, Siirola JD, Zamarripa MA, Gunter D, Shinn JH, Dowling AW, Bhattacharyya D, Biegler LT, Burgard AP, Miller DC. The idaes process modeling framework and model library—flexibility for process simulation and optimization. J Adv Manuf & Process 3: (2021). https://doi.org/10.1002/amp2.10095
4. Bellusci M, Masi A, Albino M, Peddis D, Petrecca M, Sangregorio C, La Barbera A, Varsano F. Fe3o4@hkust-1 magnetic composites by mechanochemical route for induction triggered release of carbon dioxide. Microporous and Mesoporous Materials 328:111458 (2021). https://doi.org/10.1016/j.micromeso.2021.111458
5. Ga S, An N, Joo C, Kim J. Pyapep: an all-in-one software package for the automated preparation of adsorption process simulations. Computer Physics Communications 291:108830 (2023). https://doi.org/10.1016/j.cpc.2023.108830
6. Fixed bed 1d reactor — IDAES v2.8.0. [Accessed: Nov. 7 2025] https://idaes-pse.readthedocs.io/en/2.8.0/reference_guides/model_libraries/gas_solid_contactors/unit_models/fixed_bed_1D.html
7. Adams II TA, Barton PI. A dynamic two-dimensional heterogeneous model for water gas shift reactors. International Journal of Hydrogen Energy 34:8877-8891 (2009). https://doi.org/10.1016/j.ijhydene.2009.08.045
8. Rosensweig RE. Heating magnetic fluid with alternating magnetic field. Journal of Magnetism and Magnetic Materials 252:370-374 (2002). https://doi.org/10.1016/s0304-8853(02)00706-0
9. Déjardin JL, Vernay F, Kachkachi H. Specific absorption rate of magnetic nanoparticles: nonlinear AC susceptibility. Journal of Applied Physics 128: (2020). https://doi.org/10.1063/5.0018685
10. Informatics NO of D and. NIST chemistry webbook. [Accessed: Nov. 8, 2025] https://webbook.nist.gov/chemistry/
11. Green DW, Southard MZ Eds. Perry's Chemical Engineers' Handbook. 9th Edition Edition. McGraw-Hill Education (2019). ISBN 978-0-07-183408-7
12. Wilke CR. A viscosity equation for gas mixtures. The Journal of Chemical Physics 18:517-519 (1950). https://doi.org/10.1063/1.1747673
13. Bynum ML, Hackebeil GA, Hart WE, Laird CD, Nicholson BL, Siirola JD, Watson J-P, Woodruff DL. Pyomo — Optimization Modeling in Python. Springer International Publishing (2021). ISBN 978-3-030-68927-8. https://doi.org/10.1007/978-3-030-68928-5
14. Wächter A, Biegler LT. On the implementation of an interior-point filter line-search algorithm for large-scale nonlinear programming. Math. Program. 106:25-57 (2005). https://doi.org/10.1007/s10107-004-0559-y
15. Abhyankar S, Brown J, Constantinescu EM, Ghosh D, Smith BF, Zhang H. PETSc/ts: a modern scalable ode/dae solver library. arXiv (2018). https://doi.org/10.48550/arXiv.1806.01437
16. Joss L, Gazzani M, Mazzotti M. Rational design of temperature swing adsorption cycles for post-combustion CO2 capture. Chemical Engineering Science 158:381-394 (2017). https://doi.org/10.1016/j.ces.2016.10.013
17. Glueckauf E, Coates JI. 241. theory of chromatography. part IV. the influence of incomplete equilibrium on the front boundary of chromatograms and on the effectiveness of separation. J. Chem. Soc. :1315 (1947). https://doi.org/10.1039/jr9470001315
18. Shafeeyan MS, Wan Daud WMA, Shamiri A. A review of mathematical modeling of fixed-bed columns for carbon dioxide adsorption. Chemical Engineering Research and Design 92:961-988 (2014). https://doi.org/10.1016/j.cherd.2013.08.018